The Astrophysical Journal, 901:84 (11pp), 2020 September 20 https://doi.org/10.3847/1538-4357/abafa4

A Mechanistic Study on the Formation of Acetic Acid (CH_3COOH) in Polar Interstellar Analog Ices Exploiting Photoionization Reflectron Time-of-flight Mass Spectrometry

N. Fabian Kleimeier[1,2], André K. Eckhardt[3], and Ralf I. Kaiser[1,2]
[1] Department of Chemistry, University of Hawaii at Mānoa, Honolulu, HI 96822, USA; ralfk@hawaii.edu
[2] W. M. Keck Laboratory in Astrochemistry, University of Hawaii at Mānoa, Honolulu, HI 96822, USA
[3] Department of Chemistry, Massachusetts Institute of Technology, Cambridge, MA 02139, USA
Received 2020 June 30; revised 2020 August 13; accepted 2020 August 15; published 2020 September 24

Abstract

Acetic acid (CH_3COOH) is considered a key molecule in the formation of the simplest amino acid, glycine, and consequently peptides. It is ubiquitous in the interstellar medium and has been detected toward hot cores, in the coma of comets, and on the surface of the comet 67P/Churyumov–Gerasimenko by the Rosetta mission. Here we present the isomer-selective formation of acetic acid in polar ice mixtures of water/acetaldehyde upon exposure to ionizing radiation in the form of energetic electrons as a proxy for secondary electrons generated once Galactic cosmic rays pass through interstellar ices. Acetic acid is formed even at low irradiation doses of only 0.13 eV molecule^{-1} (deuterium oxide) and 0.29 eV molecule^{-1} (acetaldehyde), representing molecular cloud lifetimes of 1×10^6 yr. Isotopic substitutions reveal that the dominant formation pathway is the barrierless radical–radical recombination of acetyl (CH_3CO) with hydroxyl-d_1 radicals (OD), whereas oxygen insertion does not yield any detectable amounts of acetic acid. This hitherto unknown reaction pathway will influence the relative abundances of distinct $C_2H_4O_2$ isomers in chemical models aiming to constrain the reaction conditions by comparing these abundances. In contrast to its formation in nonpolar model ices, the formation in this polar binary ice is isomer-selective and produces acetic acid only.

Unified Astronomy Thesaurus concepts: Laboratory astrophysics (2004); Interdisciplinary astronomy (804); Chemical abundances (224); Astrochemistry (75); Interstellar molecules (849)

1. Introduction

Ever since the observation of acetic acid (CH_3COOH) by Mehringer et al. (1997) in low- and high-mass star-forming regions toward Sgr B2(N-LMH) with abundances relative to molecular hydrogen of $(3.4 \pm 2.6) \times 10^{-10}$, the acetic acid molecule has received considerable attention from the laboratory astrophysics and astrobiology communities as a potential precursor to the simplest amino acid, glycine (H_2NCH_2COOH) (Figure 1), which can lead to dipeptides (Kaiser et al. 2013). Along with its structural isomers glycolaldehyde ($HCOCH_2OH$) and methyl formate ($HCOOCH_3$) (Bennett & Kaiser 2007a; Mottl et al. 2007; Kim & Kaiser 2010; Puletti et al. 2010; Shiao et al. 2010; Guan et al. 2012; Burke et al. 2014; Favre et al. 2017; Zhu et al. 2018), this isomer triplet has played a fundamental role in defining the (isomer-selective) fundamental chemical processes involved in the formation of complex organic molecules (COMs) in the interstellar medium (ISM). The higher energy enolic forms of acetic acid and glycolaldehyde have not yet been detected in the ISM even though it has been shown previously that the non-equilibrium chemistry triggered by Galactic cosmic rays (GCRs) can lead to a production rate of enols orders of magnitude higher than predicted from thermal equilibrium conditions (Abplanalp et al. 2016). In laboratory studies, the enol form of glycolaldehyde was tentatively assigned in methanol–carbon monoxide ice subjected to energetic electrons (Maity et al. 2014, 2015) and detected as an unstable decomposition product of norbornene precursors in a molecular-flow oven (Tureček & Havlas 1986); 1,1-ethenediol, the enolic form of acetic acid, was recently detected for the first time after flash vacuum pyrolysis of malonic acid at elevated temperature (Mardyukov et al. 2020).

Acetic acid represents the methyl derivative of formic acid (HCOOH) (Bennett et al. 2011) and is ubiquitous in hot molecular cores such as W51e2 (Remijan et al. 2002) (1.7×10^{-9}), G34.3 + 0.2 (Remijan et al. 2003), G19.61–0.23 (Shiao et al. 2010), IRAS 16293–2422 (Jørgensen et al. 2016), the Orion–KL nebula (Favre et al. 2017), and NGC 6334I (Xue et al. 2019). In our solar system, the Rosetta mission detected acetic acid on the surface of the comet 67P/Churyumov–Gerasimenko (Altwegg et al. 2017; Schuhmann et al. 2019) at concentrations of 0.0034%. Upper limits were previously proposed at levels of 0.06% compared to water for the comet C/1996 O1 (Hale–Bopp) (Crovisier et al. 2004). Nevertheless, the pathways leading to the formation of acetic acid have not been fully understood yet. Early gas-phase and grain surface chemistry has been deemed too inefficient to match astronomical observations (Garrod et al. 2008; Bergantini et al. 2017). The limits of gas-phase ion–molecule networks are well established, and complex networks such as the radiative associations ($CH_3CO^+ + H_2O \rightarrow CH_3COOH_2^+$) followed by postulated dissociative recombination with an electron ($CH_3COOH_2^+ + e^- \rightarrow CH_3COOH + H$) often rely on unstudied reactions with mainly assumed rate constants and yields, even neglecting any isomer-specific production routes. These limits are also valid for the suggested formation via the sequence $CH_3OH_2^+ + HCOOH \rightarrow CH_3COOH_2^+ + H_2O$ followed by the reaction $CH_3COOH_2^+ + e^- \rightarrow CH_3COOH + H$ (Ehrenfreund & Charnley 2000). Fang et al. (2002) pointed out the possibility of gas-phase neutral–neutral reactions via radical–radical recombination pathways (reactions (1) and (2) below). However, bimolecular reactions in the gas phase cannot dissipate the internal energy originating from C–O bond formation in the reaction intermediates. Therefore, even if acetic acid is formed as a collision complex, it will undergo unimolecular dissociation in the absence of a third-body collision event. Consequently, gas-phase-only reaction

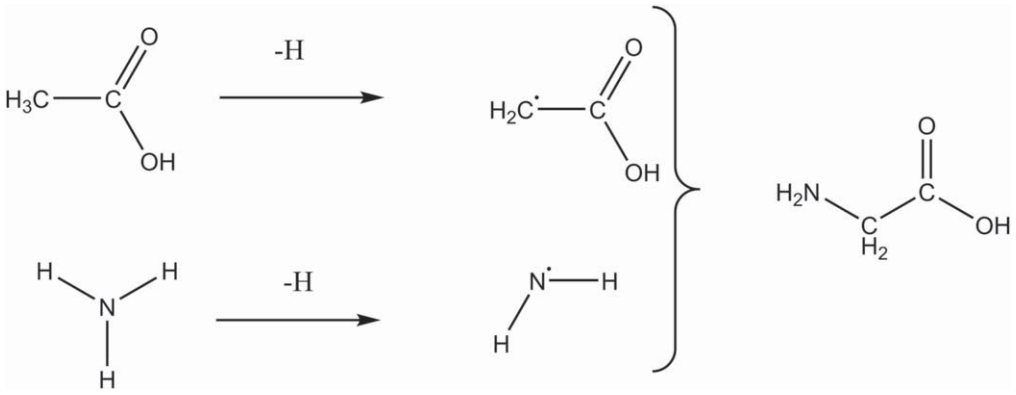

Figure 1. Possible reaction pathway for the formation of glycine from acetic acid and ammonia in interstellar ices.

networks revealed a relative abundance of acetic acid in, e.g., Sgr B2 of 2×10^{-11} (Wlodarczak & Demaison 1988), which is orders of magnitude lower than the observations (Remijan et al. 2002). Further, Mehringer et al. (1997) and Remijan et al. (2002) suggested that, based on the velocity of acetic acid in Sgr B2, its formation is linked to icy grains and hence interstellar ices.

$$CH_3CO + OH \rightarrow CH_3COOH \quad (1)$$

$$CH_3 + HOCO \rightarrow CH_3COOH. \quad (2)$$

Exploiting interstellar model ices, Bennett & Kaiser (2007a), Kim & Kaiser (2010), Zhu et al. (2018), and Bergantini et al. (2018b) revealed that acetic acid can be formed via the radical–radical recombination of methyl (CH_3) with hydroxycarbonyl (HOCO) (reaction (2)) in apolar ices containing carbon dioxide (CO_2) and methane (CH_4) exposed to ionizing radiation in the form of GCR proxies (electrons). The reaction is initiated by the decomposition of methane to form a methyl radical plus a suprathermal hydrogen atom; if the latter has sufficient energy to overcome the barrier of 113 kJ mol^{-1} (1.17 eV) to addition to the carbon dioxide molecule, the hydroxycarbonyl radical (HOCO) is formed (Zhu et al. 2001). This species reacts barrierlessly with a methyl radical to form acetic acid if both radicals have a favorable recombination geometry within the low-temperature matrix. The overall reaction to form acetic acid from methane and carbon dioxide is endoergic by 41.8 kJ mol^{-1} (0.43 eV) (Fang et al. 2002), highlighting the need for non-equilibrium (suprathermal) reactions to supply the energy required for reaction, e.g., via GCRs (Roessler 1992; Kaiser & Roessler 1997, 1998; Kaiser et al. 1997).

Nevertheless, although the aforementioned reactions nicely account for the formation of acetic acid in apolar ices, the majority of interstellar ices are water-rich and hence polar (Gibb et al. 2004). It has previously been demonstrated that glyoxylic acid (HCOCOOH), another C_2 carboxylic acid, can be formed in binary polar ices of water (H_2O) and carbon monoxide (CO) by electron irradiation (Eckhardt et al. 2019). In the present work, we exploit single-photon photoionization (PI) coupled with a reflectron time-of-flight mass spectrometer (ReTOF-MS) to explore the extent to which acetic acid can be formed inside polar, water-dominated ices doped with acetaldehyde (CH_3CHO) upon exposure to ionizing radiation in the form of energetic electrons. These electrons replicate secondary electrons released in the track of GCRs penetrating interstellar ices (Kaiser & Roessler 1997, 1998; Bennett et al. 2005a; Alizadeh et al. 2015). Considering the facile formation of acetaldehyde in interstellar and solar system analog ices (Moore & Hudson 1998; Bennett et al. 2005a, 2005b; Öberg et al. 2009, 2010; Kaiser et al. 2014), it is not surprising that acetaldehyde has been detected throughout the ISM in the gas phase, ranging from cold molecular clouds such as TMC-1 to warmer envelopes around star-forming regions, e.g., Sgr B2 (Fourikis et al. 1974; Matthews et al. 1985), hot cores such as NGC 6334F (Nummelin et al. 1998), and quiescent regions such as CB 17 (Turner et al. 1999). Furthermore, tentative detections of acetaldehyde in interstellar ices have been published with upper limits of 3% (Schutte et al. 1998, 1999) and 10% (Gibb et al. 2004) relative to water. In our solar system, acetaldehyde was detected in meteorites such as Murchison (Jungclaus et al. 1976), in comets such as Hale–Bopp (Crovisier et al. 2004), and during the Rosetta mission on 67P/Churyumov–Gerasimenko (Altwegg et al. 2017). Since PI-ReToF-MS is very sensitive and represents an isomer-selective detection method, experiments at doses as low as (0.13 ± 0.03) eV $molecule^{-1}$ of water and (0.29 ± 0.05) eV $molecule^{-1}$ of acetaldehyde were carried out. This resembles the average dose deposited by cosmic rays over 10^6 yr inside typical molecular clouds (Yeghikyan 2011). These studies deliver much required fundamental, mechanistic information on the *very early phases* involved in the synthesis of carboxylic acids in interstellar ices at temperatures as low as 10 K.

2. Experiment

2.1. Experimental Strategy

Considering the molecular structure of acetic acid along with its adiabatic ionization energies and its structural isomers (Table 1), we pursue the following strategy to investigate the formation of this carboxylic acid in acetaldehyde-doped water ices (Figure 2). Here, exploiting acetaldehyde (CH_3CHO)–deuterium oxide (D_2O) ices with a ratio of 1:10 critically assists in elucidating the dominating reaction mechanisms. Deuterium oxide was chosen because different reaction mechanisms will result in different mass-to-charge ratios of the products investigated. Upon interaction with ionizing radiation, the deuterium oxide molecule can decompose via simple rupture of the oxygen–deuterium bond, leading to atomic deuterium and the hydroxyl-d_1 radical (OD) (reaction (3)), or via molecular deuterium loss accompanied by the formation of electronically excited atomic oxygen ($O(^1D)$) (reaction (4)) (Zheng et al. 2006a, 2006b, 2007). The hydroxyl-d_1 radical can undergo barrierless radical–radical recombination reactions with fragments of the radiolyzed

Table 1
Computed Adiabatic Ionization Energies (IE_{calc}), Experimental Ionization Energies (IE_{exp}), and Relative Energies for $C_3H_4O_3$ Isomers

	Name	IE_{calc} /eV	IE_{exp} /eV	Point group	Electronic state	Relative energy / kJ mol^{-1}
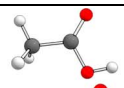	*anti*-acetic acid	10.65	10.65 ± 0.02[1]	C_s	^{1}A'	0.0
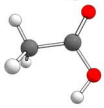	*syn*-acetic acid	10.52		C_s	^{1}A'	20.8
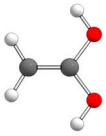	*syn, syn*-1,1-ethenediol	8.68		C_{2v}	^{1}A$_1$	117.1
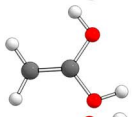	*syn, anti*-1,1-ethenediol	8.58		C_s	^{1}A'	112.3
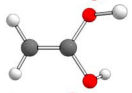	*anti, anti*-1,1-ethenediol	8.59		C_2	^{1}A	124.6
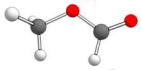	*anti*-methyl formate	10.68	10.835[1]	C_s	^{1}A'	93.3
	*syn*-methyl formate	10.83		C_s	^{1}A'	72.6
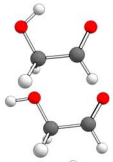	*syn*, *syn*-glycolaldehyde	10.06		C_s	^{1}A'	112.9
	syn, *anti*-glycolaldehyde	9.84	9.95 ± 0.05[2]	C_s	^{1}A'	133.5
	*anti*, *anti*-glycolaldehyde	9.91		C_s	^{1}A'	125.5
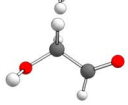	*anti*, *gauche*-glycolaldehyde	9.90		C_1	^{1}A	127.0
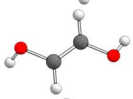	*E-anti-anti*-1,2-ethenediol	8.16		C_2	^{1}A	167.2
	*E-syn-anti*-1,2-ethenediol	8.30		C_1	^{1}A	166.3
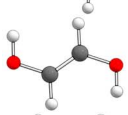	*E-syn-syn*-1,2-ethenediol	8.41	9.62 ± 0.04[3]	C_2	^{1}A	165.0
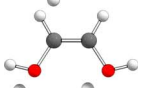	*Z-anti-anti*-1,2-ethenediol	8.21		C_{2v}	^{1}A$_1$	162.9
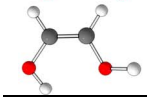	*Z-syn-anti*-1,2-ethenediol	8.37		C_1	^{1}A	146.9

acetaldehyde molecule: the acetyl radical (CH_3CO; reaction (5)) and the vinoxy radical (CH_2CHO; reaction (6)). These radical–radical pathways may lead to the formation of acetic acid-d_1 (CH_3COOD, reaction (7); 61 amu) and glycolaldehyde-d_1 ($HCOCH_2OD$, reaction (8); 61 amu), respectively (Figure 2). On the other hand, electronically excited atomic oxygen ($O(^1D)$) may insert into carbon–hydrogen and carbon–carbon single bonds, leading to glycolaldehyde ($HCOCH_2OH$, reaction (9); 60 amu), methyl formate ($HCOOCH_3$, reaction (10); 60 amu), and acetic acid (CH_3COOH, reaction (11); 60 amu). Consequently, the radical–radical recombination and the oxygen insertion pathways can be discriminated based on the appearance

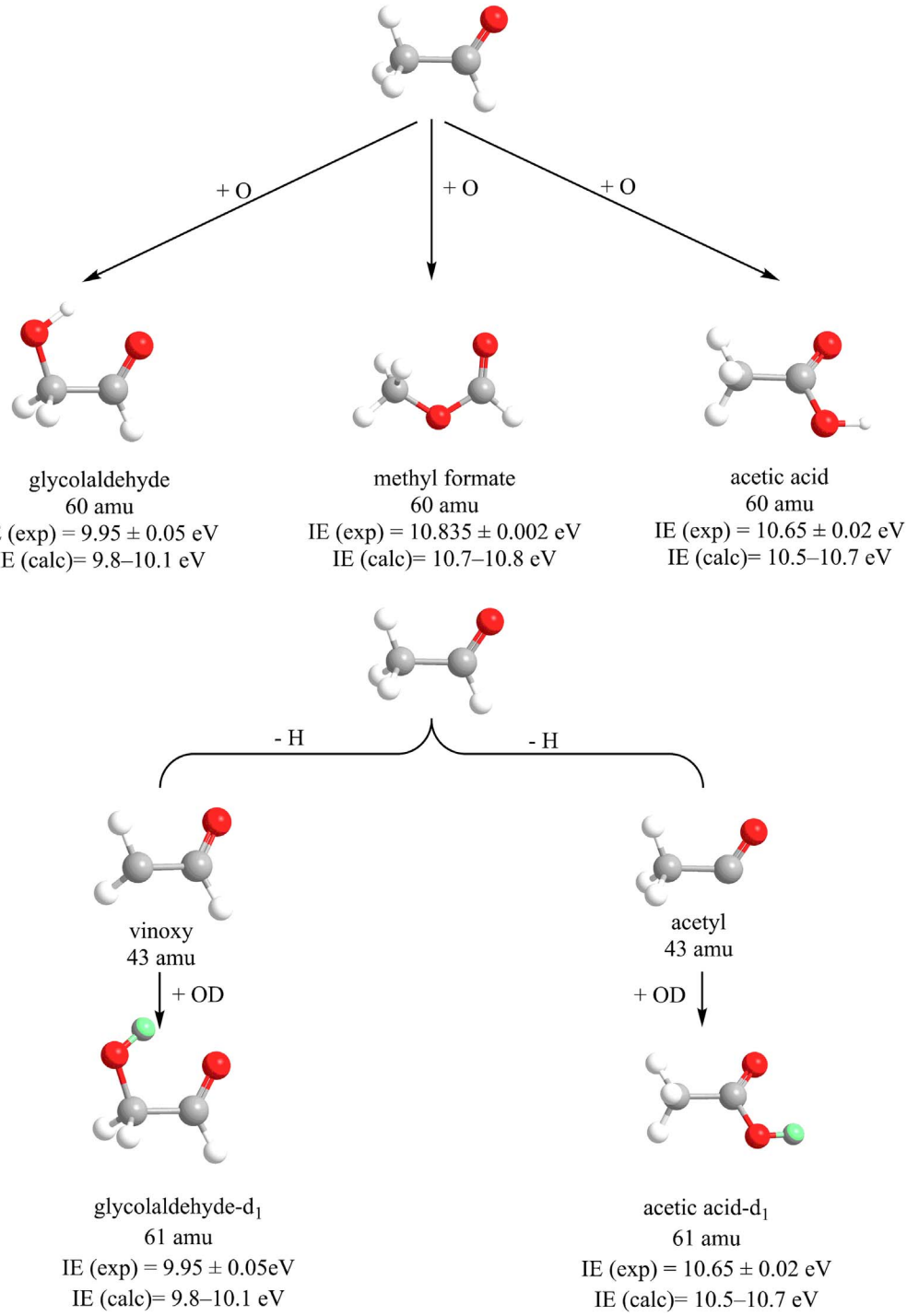

Figure 2. A radical–radical reaction between the hydroxyl-d_1 radical and the acetyl and vinoxy radicals yields glycolaldehyde-d_1 ($m/z = 61$) and acetic acid-d_1 ($m/z = 61$), respectively, along with their enolic forms. Oxygen insertion into distinct single bonds of the acetaldehyde molecule yields glycolaldehyde ($m/z = 60$), methyl formate ($m/z = 60$), and acetic acid ($m/z = 60$) along with their enolic isomers.

of products with molecular masses of 61 and 60 amu, respectively. Isomers can be discriminated selectively based on the unique adiabatic ionization energies (Table 1).

$$D_2O \rightarrow D + OD \quad (\Delta_r G = 499 \text{ kJ mol}^{-1}, 5.17 \text{ eV}) \quad (3)$$

$$D_2O \rightarrow D_2 + O(^1D) \quad (\Delta_r G = 679 \text{ kJ mol}^{-1}, 7.04 \text{ eV}) \quad (4)$$

$$CH_3CHO \rightarrow CH_3CO + H \quad (\Delta_r G = 377 \text{ kJ mol}^{-1}, 3.91 \text{ eV}) \quad (5)$$

$$CH_3CHO \rightarrow CH_2CHO + H \quad (\Delta_r G = 411 \text{ kJ mol}^{-1}, 4.26 \text{ eV}) \quad (6)$$

$$CH_3CO + OD \rightarrow CH_3COOD \quad (\Delta_r G = -461 \text{ kJ mol}^{-1}, -4.78 \text{ eV}) \quad (7)$$

$$CH_2CHO + OD \rightarrow HCOCH_2OD \quad (\Delta_r G = -383 \text{ kJ mol}^{-1}, -3.97 \text{ eV}) \quad (8)$$

Table 2
Overview of Experimental Conditions

Ice	Ratio D_2O:CH_3CHO	Thickness (nm)	Current (nA)	Irradiation Time (s)	Dose (eV molecule^{-1}) D_2O	Dose (eV molecule^{-1}) CH_3CHO	Photon Energy (eV)
I	13 ± 3 : 1	950 ± 200	…	…	…	…	10.86
II	9 ± 2 : 1	950 ± 50	20 ± 1	900	0.5 ± 0.1	1.2 ± 0.2	10.86
III	8 ± 2 : 1	950 ± 100	15 ± 1	300	0.13 ± 0.03	0.28 ± 0.05	10.86
IV	9 ± 2 : 1	1000 ± 200	15 ± 1	300	0.13 ± 0.03	0.29 ± 0.05	10.28
V	10 ± 2 : 1	950 ± 50	15 ± 1	300	0.13 ± 0.03	0.29 ± 0.05	10.72

$$CH_3CHO + O(^1D) \rightarrow HCOCH_2OH \quad (\Delta_r G = -588\ \text{kJ mol}^{-1}, -6.09\ \text{eV}) \quad (9)$$

$$CH_3CHO + O(^1D) \rightarrow CH_3OCHO \quad (\Delta_r G = -602\ \text{kJ mol}^{-1}, -6.24\ \text{eV}) \quad (10)$$

$$CH_3CHO + O(^1D) \rightarrow CH_3COOH \quad (\Delta_r G = -699\ \text{kJ mol}^{-1}, -7.25\ \text{eV}) \quad (11)$$

$$CH_3CHO + D_2O \rightarrow CH_3COOD + H + D \quad (\Delta_r G = 415\ \text{kJ mol}^{-1}, 4.30\ \text{eV}). \quad (12)$$

2.2. Experimental Procedure

Experiments were conducted in ultrahigh vacuum (UHV) conditions at pressures of a few 10^{-11} Torr inside a stainless steel chamber that has been described in detail by Jones & Kaiser (2013). A polished silver substrate was interfaced to a two-stage closed-cycle helium cryostat that can be freely rotated and translated vertically. Acetaldehyde (Sigma Aldrich, p.a., anhydrous, ⩾99.5%)—purified by trap-to-trap distillation—and deuterium oxide (Cambridge Isotope Laboratories, Inc., >99.96% D) were stored in separate glass vials interfaced to a UHV chamber and subjected to several freeze–thaw cycles using liquid nitrogen to remove residual atmospheric gases. After cooling the substrate to 5 K, acetaldehyde and deuterium oxide vapors were simultaneously deposited exploiting separate glass capillary arrays. To achieve a ratio of deuterium oxide to acetaldehyde in the ice of 10:1, the partial pressures of deuterium oxide and acetaldehyde during the deposition were chosen to be 3×10^{-8} Torr and 5×10^{-9} Torr, respectively, and they were monitored using a quadrupole residual gas analyzer (RGA; Extrel 5221). The overall thickness of the ice was monitored by recording interference fringes between the reflections of a helium–neon laser off the silver substrate and the ice surface with a photodiode as described by Turner et al. (2015). The concentration-weighted average between the refractive index of amorphous water ice ($n = 1.29 \pm 0.01$) (Dohnálek et al. 2002) and that of acetaldehyde ($n = 1.303$) (Hudson & Coleman 2019) of 1.29 ± 0.01 was used to derive the thickness of the ices from the interference fringes. Thicknesses of about 1000 nm were chosen to prevent electrons from reaching the silver substrate. Subsequently, the ice composition was determined by integrating the acetaldehyde infrared features at 3006, 1428, 1350, and 1128 cm^{-1} and exploiting absorption coefficients of $A_{exp} = 5.1 \times 10^{-19}$, 1.9×10^{-18}, 1.1×10^{-18}, and 6.6×10^{-19} cm molecule^{-1} as determined in our setup under identical geometrical conditions via calibration experiments exploiting pure acetaldehyde ices. The thickness of the ices was determined by laser interferometry, so the column density of deuterium oxide was determined from the difference between the thickness derived for acetaldehyde and the known thickness of the ice. The results of this analysis are summarized in Table 2 along with experimental parameters.

Table 3
Wavelengths Used to Generate the Different Photon Energies of the Photoionization Source

	Photon energy (eV)	10.86	10.72	10.28
	Wavelength (nm)	114.2	115.72	120.6
ω_1	Wavelength (nm)	202.316	202.316	202.316
Nd:YAG (ω_1)	Wavelength (nm)	532	532	532
Dye laser (ω_1)	Wavelength (nm)	606.948	606.948	606.948
Dye (ω_1)[a]		Rh mix	Rh mix	Rh mix
ω_2	Wavelength (nm)	888	807	627
Nd:YAG (ω_2)	Wavelength (nm)	532	532	532
Dye laser (ω_2)	Wavelength (nm)	888	807	627
Dye (ω_2)[a]		LDS 867	LDS 798	Rh 640

Note.
[a] Rh mix: Rhodamine 610 + Rhodamine 640; Rh 640: Rhodamine 640.

After the deposition, the ice was subjected to 5 keV electron irradiation for 5 minutes at 15 nA by rastering an electron beam over the entire sample. The irradiation current was measured before and after irradiation using a Faraday cup that was inserted into the beam path. These irradiation conditions correspond to doses of (0.29 ± 0.04) eV molecule^{-1} and (0.13 ± 0.03) eV molecule^{-1} for acetaldehyde and deuterium oxide, respectively, according to Monte Carlo simulations carried out in the CASINO software suite (Drouin et al. 2007). Additionally, one experiment was carried out at higher doses of (1.2 ± 0.2) eV molecule^{-1} (acetaldehyde) and (0.5 ± 0.1) eV molecule^{-1} (deuterium oxide) to facilitate the detection of changes in the IR spectrum after the irradiation. Subsequent to the irradiation, temperature-programmed desorption (TPD) studies were conducted by heating the sample at a rate of 0.5 K minute^{-1} up to 300 K. Molecules subliming from the sample were analyzed by photoionization reflectron time-of-flight mass spectrometry (PI-ReToF-MS) to minimize fragmentation of the ionized species. The tunable vacuum ultraviolet (VUV) light used in this study was generated by resonant four-wave mixing of two synchronized pulsed dye lasers (Sirah, Cobra-Stretch) pumped by two Nd:YAG lasers (Spectra Physics, Quanta Ray Pro 250-30 and 270-30) operating at a repetition rate of 30 Hz (Hilbig & Wallenstein 1983). The lasers were spatially and temporally overlapped inside a pulsed valve backed with krypton at a pressure of 2000 Torr and tuned to the wavelengths needed to generate the desired VUV photon energy (Table 3). A biconvex lithium fluoride (LiF) lens in an off-axis geometry was utilized to separate the VUV photons from the dye laser output and to focus the VUV light. After passing through a 1 mm aperture, the VUV

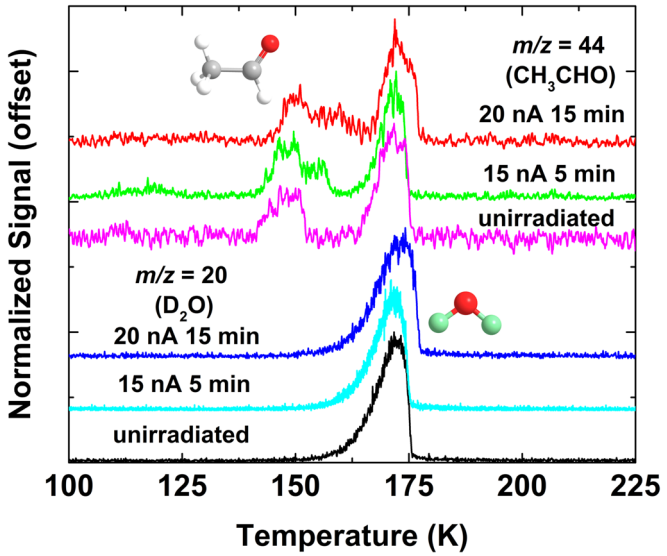

Figure 3. TPD profiles for deuterium oxide ($m/z = 20$, lower traces) and acetaldehyde ($m/z = 44$, upper traces) for different doses of electron irradiation. The $m/z = 44$ traces have been smoothed with a moving average at intervals of 0.5 K.

photons entered the UHV chamber and passed in front of the silver substrate to ionize subliming molecules. The resulting ions were then analyzed using a ReToF-MS (Jordan TOF Products, Inc.) according to their arrival times in bins 4 ns wide. Integration times were set to 2 minutes to record mass spectra in 1 K intervals during the TPD phase. Because reactant molecules often exhibit higher ionization energies than the cutoff energy of the LiF lens (11.1 eV) or saturate the detector of the ReToF-MS, the quadrupole mass spectrometer was used to monitor the sublimation of reactant molecules during the TPD phase. The traces recorded at different electron irradiation doses for both deuterium oxide ($m/z = 20$) and acetaldehyde ($m/z = 44$) are shown in Figure 3, obtained with an electron current of 2.0 mA and electron energy of 70 eV in the electron impact ionizer. In the unirradiated ice, two desorption events are seen for the acetaldehyde molecule ($m/z = 44$). One of these events corresponds to the desorption temperature of pure acetaldehyde samples, whereas the second desorption event at 156 K corresponds to codesorption with the water matrix. Additionally, after irradiation, another desorption event emerges between the two peaks, which gets broader at the higher irradiation dose. This desorption event and its broadening can be attributed to the formation of acetaldehyde polymers as seen previously for pure acetaldehyde ices (Kleimeier et al. 2020). In contrast, no dependence on the electron irradiation is found for the deuterium oxide desorption profile at $m/z = 20$.

2.3. Computational Methods

All computations were carried out with Gaussian 16, Revision A.03 (Frisch et al. 2016). For geometry optimizations and frequency computations, the density functional theory (DFT) B3LYP functional (Becke 1988, 1993; Lee et al. 1988) was employed utilizing the Dunning correlation-consistent split valence basis set cc-pVTZ (Dunning 1989). Based on these geometries, the corresponding frozen-core coupled cluster (Bartlett et al. 1990; Raghavachari 1991; Čížek 1966; Stanton 1997) CCSD(T)/cc-pVDZ, CCSD(T)/cc-pVTZ, and CCSD(T)/cc-pVQZ single-point energies were computed and extrapolated to the complete basis set limit (Peterson et al. 1994) CCSD(T)/CBS with B3LYP/cc-pVTZ zero-point vibrational energy (ZPVE) corrections. The adiabatic ionization energies were computed by taking the ZPVE corrected energy difference between the neutral and ionic species that correspond to similar conformations. Calculations performed for a small subset of the molecules using the computationally more expensive augmented basis sets at the same zeta level revealed that they did not affect the ionization energies to the significant figures reported and only had a marginal effect on the relative energies (<2.5 kJ mol^{-1}). Therefore, the cc-pVTZ basis set is sufficient for the present purposes and was utilized for all molecules to save computation time without sacrificing the required accuracy.

Furthermore, the difference in deuterated and non-deuterated isotopologues in the ZPVE is generally marginal so we used the ZPVEs of non-deuterated isotopologues for *IE* calculations and assume them to be the same for our experiments with heavier isotopologues. The experimental ionization energies of glycolaldehyde (9.95 ± 0.05 eV) (Porterfield et al. 2016), methyl formate (10.835 ± 0.002 eV) (Lias 2020), and acetic acid (10.65 ± 0.02 eV) (Lias 2020) agree well with the computed adiabatic ionization energies, being systematically too low by 0.11 eV to 0.15 eV for each isomer considering the conformers with the lowest calculated ionization energy for each isomer (Table 1).

3. Results and Discussion

3.1. FTIR

The Fourier transform infrared (FTIR) spectra of the deuterium oxide/acetaldehyde ice mixture before and after the electron irradiation are shown in Figure 4. Before the irradiation, the absorptions can be attributed to acetaldehyde and deuterium oxide with a small contamination of water as compiled in Table 4. This contamination is most likely due to H/D exchange reactions inside the gas deposition system because it exceeds the level of the specified isotopic purity and is detected by the RGA in the gas phase during deposition. After the irradiation, the absorbance features of acetaldehyde (ν_1, ν_5, ν_7, and ν_8) and deuterium oxide (ν_2) decreased by (12 ± 2)% and 8%, respectively. As the OD stretching region (2100–2800 cm^{-1}) is not unique to deuterium oxide and hence can overlap with OD stretches from product molecules and radicals, only the D–O–D bending mode (ν_2) was analyzed for the assessment of deuterium oxide processing. In addition to the overall decrease of signals associated with the reactant molecules, new absorption features arose at 2135 cm^{-1}, 1841 cm^{-1}, and 667 cm^{-1}, indicating formation of carbon monoxide (CO; ν_1), the acetyl radical (ν (C=O)) (Jacox 1982; Kleimeier et al. 2020), and carbon dioxide (CO_2, ν_2) respectively. Note that, as seen for pure acetaldehyde ices, no absorption features associated with the vinoxy radical (1540, 1520 cm^{-1}) were observed (Kleimeier et al. 2020). Due to overlapping IR features of multiple COMs, no other reaction products could be uniquely identified, signifying the need for an additional experimental technique to probe the *individual* reaction products.

3.2. PI-ReToF-MS—Acetic Acid

To identify individual COMs formed in the irradiation experiments, PI-ReToF-MS is exploited to analyze molecules according to their mass-to-charge ratio and ionization energies (Figure 2, Table 1). As (partial) deuteration of the molecules does not significantly alter the ionization energies at least at

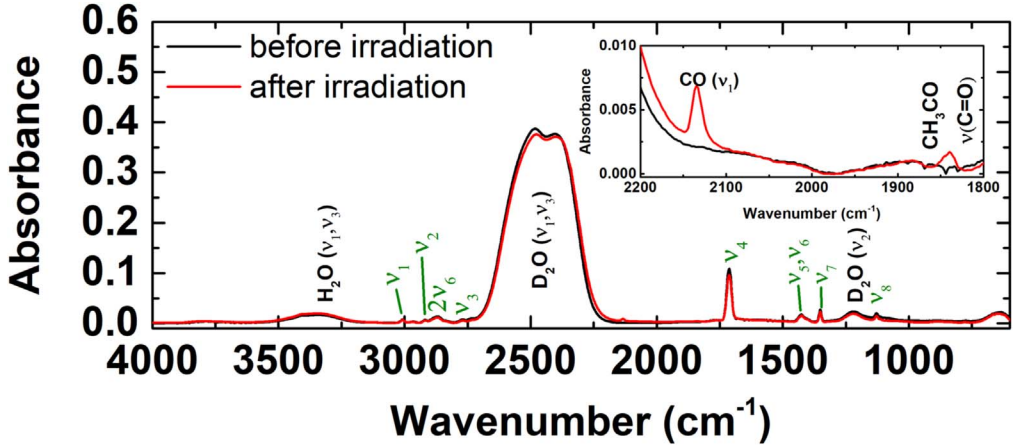

Figure 4. FTIR spectrum of the deuterium oxide/acetaldehyde ice before (black trace) and after (red trace) irradiation at 20 nA for 15 minutes. Peak assignments in green correspond to acetaldehyde. Inset: zoom in between 2200 and 1800 cm^{-1} showing new peaks after irradiation corresponding to carbon monoxide (2133 cm^{-1}) and the acetyl radical (1840 cm^{-1}).

Table 4
Observed Infrared Peaks and Assignments in Deuterium Oxide/Acetaldehyde Ices before Electron Irradiation

Absorption (cm^{-1})	Molecule	Assignment	Mode
3350	H_2O	ν_1/ν_3	$\nu_{s/as}$(HOH)
3118	CH_3CHO	$\nu_4 + \nu_6$	combination
3008	CH_3CHO	ν_1	$\nu_{as}(CH_3)$
2967	CH_3CHO	ν_{11}	$\nu(CH_3)$
2920	CH_3CHO	ν_2	$\nu_s(CH_3)$
2869	CH_3CHO	$2\nu_6$	overtone
2840	CH_3CHO	$2\nu_6$	overtone
2768	CH_3CHO	ν_3	ν(CH)
2744	CH_3CHO	ν_3	ν(CH)
2450	D_2O	$\nu_{1/3}$	$\nu_{s/as}$(DOD)
1771	CH_3CHO	$2\nu_9$	overtone
1712	CH_3CHO	ν_4	ν(C=O)
1428	CH_3CHO	ν_{12}/ν_5	$\delta(CH_3)/\delta_{as}(CH_3)$
1397	CH_3CHO	ν_6	δ(CH)
1351	CH_3CHO	ν_7	$\delta_s(CH_3)$
1220	D_2O	ν_2	δ(DOD)
1127	CH_3CHO	ν_8	$\gamma_r(CH_3)$
1110	$^{13}CH_3CHO$	ν_8	$\gamma_r(^{13}CH_3)$
774	CH_3CHO	ν_{14}	γ(CH)

levels of less than 0.01 eV (change in ZPVEs under the assumption of the Born–Oppenheimer approximation), the computed adiabatic ionization energies are also valid for (partially) deuterated products. Note that the electric field of the optics was found to decrease the adiabatic ionization energies by 0.03 eV (Bergantini et al. 2018a). Considering the known experimental ionization energies (IE_{exp}) (Figure 2) along with the computed values of unknown adiabatic ionization energies (IE_{calc}) of the remaining isomers (Table 1), experiments were carried out at distinct photon energies of the photoionization source to distinguish the isomers. The results of these studies are summarized in Figure 5, which shows the temperature-dependent mass spectra of each experiment. Note that an experiment without electron irradiation (blank) was also conducted (Figure 5, top left).

First, after the irradiation, several new ion signals were recorded at a photon energy of 10.86 eV (Figure 5, top right). A summary of all mass-to-charge ratios detected in the different experiments is given in Table 5. According to the computed and experimental ionization energies, this photon energy can ionize *all* $C_2H_4O_2$ isomers because the highest ionization energy is (10.835 ± 0.002) eV for methyl formate ($HCOOCH_3$). Details of the TPD traces for $C_2H_4O_2$ (oxygen insertion, $m/z = 60$) and $C_2DH_3O_2$ (radical–radical reaction, $m/z = 61$) are shown in the top row of Figure 6. As *no signal* can be detected at $m/z = 60$ (left), oxygen insertion did not contribute to the formation of any $C_2H_4O_2$ isomers, whereas the barrierless reaction of C_2H_3O radicals with the hydroxyl-d_1 radicals formed at least one $C_2DH_3O_2$ isomer as evidenced by the ion signal at $m/z = 61$. Considering the fact that methyl formate ($HCOOCH_3$) can only be formed via oxygen insertion and that no ion counts were detected at $m/z = 60$ for any insertion products, we can clearly rule out the formation of methyl formate ($HCOOCH_3$).

Second, by tuning the photon energy down to 10.72 eV (Figure 5, bottom left), methyl formate ($IE_{exp} = 10.835 \pm 0.002$), which was already ruled out based on the lack of any signal at $m/z = 60$, cannot be ionized anymore, but all the remaining isomers can still contribute to the ion signal recorded. As seen in the top right panel of Figure 6, ions at $m/z = 61$ were still detected with an identical desorption profile as recorded at 10.86 eV. Therefore, methyl formate—which we already excluded in the aforementioned discussion based on the lack of any ion counts at $m/z = 60$—can once again be excluded as molecule formed in the ices. Therefore, ion signal at $m/z = 61$ can only originate from (conformers of) acetic acid-d_1, glycolaldehyde-d_1 along with 1,1- and/or 1,2-ethenediol (Table 1).

Third, further reducing the photon energy to 10.28 eV (Figure 5, bottom right) eliminates the photoionization of acetic acid ($IE_{exp} = 10.65 \pm 0.02$ eV) since the photon energy is below its adiabatic ionization energy; on the other hand—if present—1, 1- and/or 1, 2-ethenediol can still contribute to the ion signal. The TPD trace shown in Figure 6 (top right) clearly reveals that no ions are detected at this photon energy. This strongly indicates that only acetic acid-d_1 (CH_3COOD) is formed in deuterium oxide–acetaldehyde ices upon electron irradiation. This is in line with the IR detection of the acetyl radical as a precursor to acetic acid, which can form barrierlessly via the radical–radical reaction of acetyl and hydroxyl radicals (reaction (7)).

Finally, an additional confirmation of the assignment of acetic acid-d_1 (CH_3COOD) is the detection of ion counts at $m/z = 63$ ($C_2H_3D_2O_2$, Figure 6, bottom left) and at $m/z = 107$ ($C_3H_3D_2O_4$, Figure 6, bottom right) with the same desorption profile. These

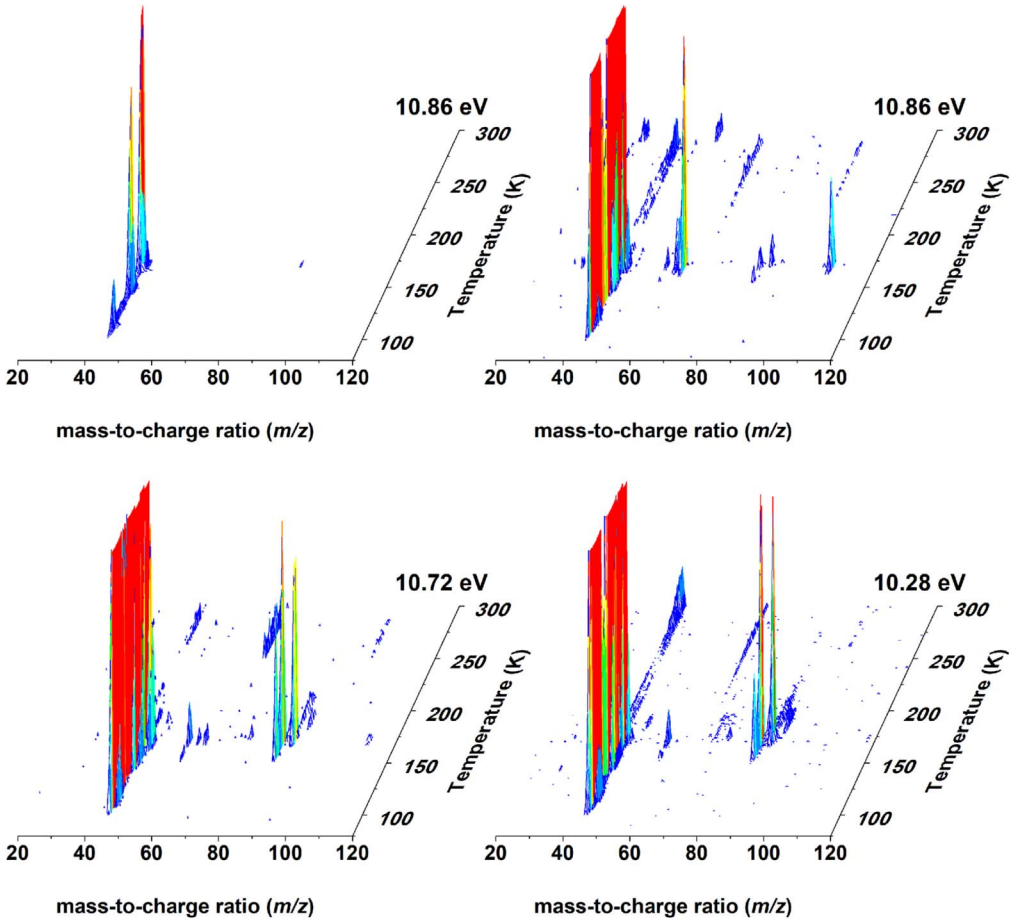

Figure 5. Top: temperature-dependent PI-ReToF mass spectra. Top panels: unirradiated deuterium oxide/acetaldehyde ice (left) and ice irradiated with 5 keV electrons at 15 nA for 5 minutes (right) recorded at 10.86 eV. Bottom panels: irradiated ice recorded at 10.72 eV (left) and 10.28 eV (right). Irradiated ices are scaled to the height of the most intense product peak.

Table 5
Mass-to-charge Ratios Not Linked to Acetic Acid Observed in Each Experiment and Assignment to Molecules

m/z	10.86 eV	10.72 eV	10.28 eV	Assignment	Ionization Energy (eV)
30	(√)[a]	×	×	H_2CO	10.88 ± 0.01
33	√	×	×	CH_3OD	10.84 ± 0.01
42	√	√	√	H_2CCO	9.617 ± 0.003
43	√	√	√	CH_3CO (fragment)	9.88/10.68[b]
44	√	√	√	CH_3CHO	10.229 ± 0.0007
45	√	√	√	$(CH_3CHO)H^+$	
46	√	√	√	$(CH_3CHO)D^+$	
58	√	√	√	CH_3COCH_3	9.703 ± 0.006
86	√	√	√	$CH_3COCOCH_3$	9.23 ± 0.03
87	√	√	√	$CH_3COCOCH_2D$	9.23 ± 0.03
88	(√)[a]	√	√	$(CH_3CHO)_2$	
89	√	√	√	$(CH_3CHO)_2H^+$	
90	(√)[a]	√	√	$(CH_3CHO)_2D^+$	
92	√	√	√	?[c]	

Notes. Ionization energies according to NIST Chemistry Webbook.
[a] Only observed in higher dose experiment at 10.86 eV (20 nA, 15 minutes).
[b] 10.68 eV for acetaldehyde, 9.88 eV for 2,3-butanedione ($CH_3COCOCH_3$).
[c] Also observed without irradiation.

mass-to-charge ratios can be associated with the two most common cationic fragments of photoionized acetic acid-d_1 dimers, $(CH_3COOD)D^+$ and $(CH_3COOD)COOD^+$, respectively. According to a study conducted by Guan et al. (2012), the parent dimer of these fragments at $m/z = 124$ fully fragments at the employed photon energies and is therefore not detected. The detection of these two fragments is also in agreement with a previous study of acetic acid formation in apolar ices by Bergantini et al. (2018b). By comparing the integrated signal intensities of CH_3COOD^+ and $(CH_3COOD)D^+$ with signal intensities of CH_3COOH^+ and

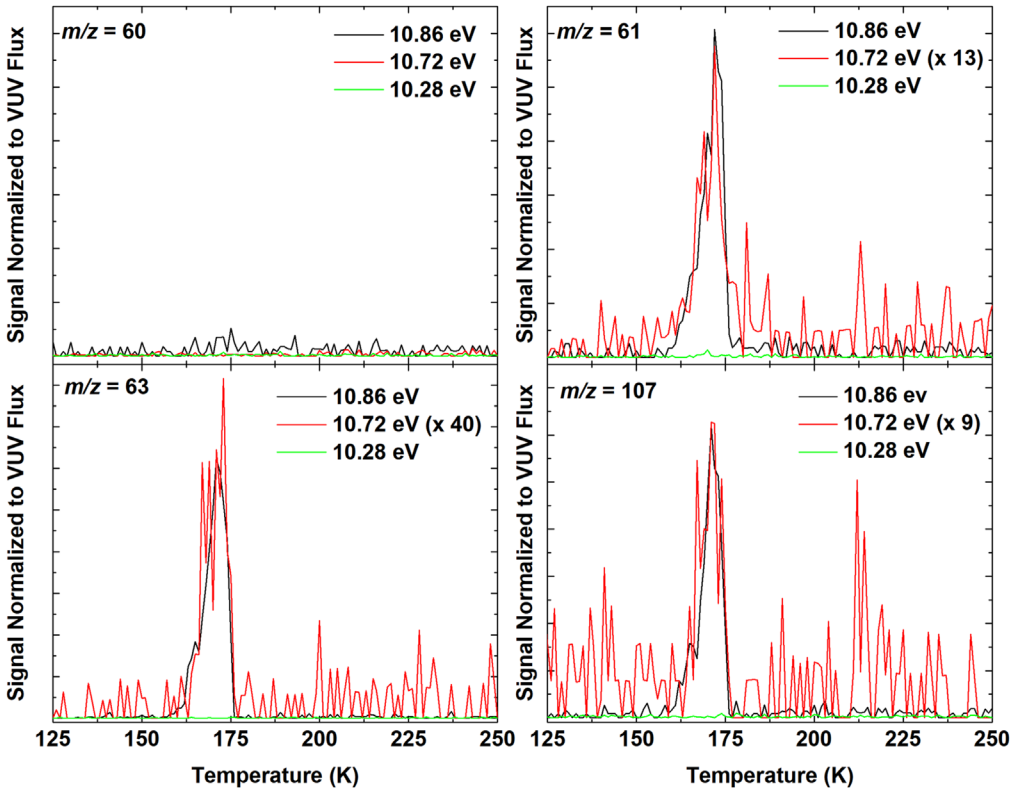

Figure 6. TPD desorption profiles of species subliming from the irradiated deuterium oxide/acetaldehyde ice recorded at different photon energies at mass-to-charge ratios corresponding to $C_2H_4O_2$ ($m/z = 60$, upper left panel), $C_2H_3DO_2$ ($m/z = 61$, upper right panel), deuteronated $(C_2H_3DO_2)D$ ($m/z = 63$, lower left panel), and $(C_2H_3DO_2)CO_2D$ ($m/z = 107$, lower right panel). Traces recorded at 10.72 eV have been scaled to the height of those recorded at 10.86 eV.

$(CH_3COOH)H^+$ obtained in calibration experiments with defined thicknesses of pure acetic acid ice, the production rate of acetic acid in the deuterium oxide/acetaldehyde ice was determined to be between a lower limit of $(8 \pm 1) \times 10^{-5}$ molecules eV^{-1} and an upper limit of $(8 \pm 1) \times 10^{-4}$ molecules eV^{-1} based on the relative signal intensities of the dimer fragment and the monomeric ion, respectively.

3.3. PI-ReToF-MS—Other Molecules

Besides acetic acid-d_1, additional molecules were detected in the experiments conducted at a photon energy of 10.86 eV (Table 5). First, a single desorption event at $m/z = 30$ was recorded, which was not seen at the lower photon energies. Based on the ice composition and the ionization energy, this molecule can be identified as formaldehyde (H_2CO, $IE_{exp} = (10.88 \pm 0.01)$ eV) (Lias 2020), which can form from the barrierless reaction of the formyl radical (HCO) with a hydrogen atom from the acetyl formation. Second, a desorption event was detected at $m/z = 33$. This mass-to-charge ratio can be associated with methanol-d_1 (CH_3OD), which has an ionization energy of (10.85 ± 0.03) eV (Tao et al. 1992). Based on the ice composition, this indicates that a methyl radical (CH_3) from the irradiation of acetaldehyde reacted with a hydroxyl-d_1 radical that formed from the deuterium oxide. All other reaction products were detected at all ionization energies employed in this study. Based on their detection in pure acetaldehyde ices after irradiation (Kleimeier et al. 2020), these molecules can be identified as ketene (CH_2CO, $m/z = 42$), protonated and deuteronated acetaldehyde ($(CH_3CHO)H^+$, $m/z = 45$ and $(CH_3CHO)D^+$, $m/z = 46$), as well as acetone (CH_3COCH_3, $m/z = 58$) and diacetyl ($CH_3COCOCH_3$, $m/z = 86$) along with diacetyl-d_1 at $m/z = 87$. Furthermore, as in pure acetaldehyde ices, the acetaldehyde dimer ($(CH_3CHO)_2$, $m/z = 88$) and its protonated and deuteronated cations at $m/z = 89$ and $m/z = 90$, respectively, were detected.

4. Astrophysical Implications and Conclusions

In this study we have demonstrated that acetic acid forms in polar interstellar ice analogues containing deuterium oxide and acetaldehyde in realistically dilute mixtures of about 10:1 through non-equilibrium chemistry after energetic processing by electron irradiation. This mimics the secondary electrons in the tracks of GCRs impinging on interstellar ice in molecular clouds. Using doses corresponding to those received by interstellar ices within 10^6 yr, which is at the lower end of typical molecular cloud lifetimes, appreciable amounts of acetic acid were detected. Following gravitational collapse and subsequent warming of the cloud, the acetic acid sublimes and can form dimers as is evident from the fragments detected in this study. As the polar layer of interstellar ice also contains ammonia (Öberg et al. 2011), further energetic processing to form the amino acid glycine or more complex biomolecules is conceivable. During star formation, these molecules can be incorporated into planets, planetoids, comets, and asteroids, which can eventually deliver them to planets, constituting an exogenous source of biomolecules.

In contrast to formation pathways in apolar ices such as methane–carbon dioxide, in which both glycolaldehyde and acetic acid were found to form upon irradiation (Bergantini et al. 2018b) or the polar–nonpolar mixture of methanol–carbon

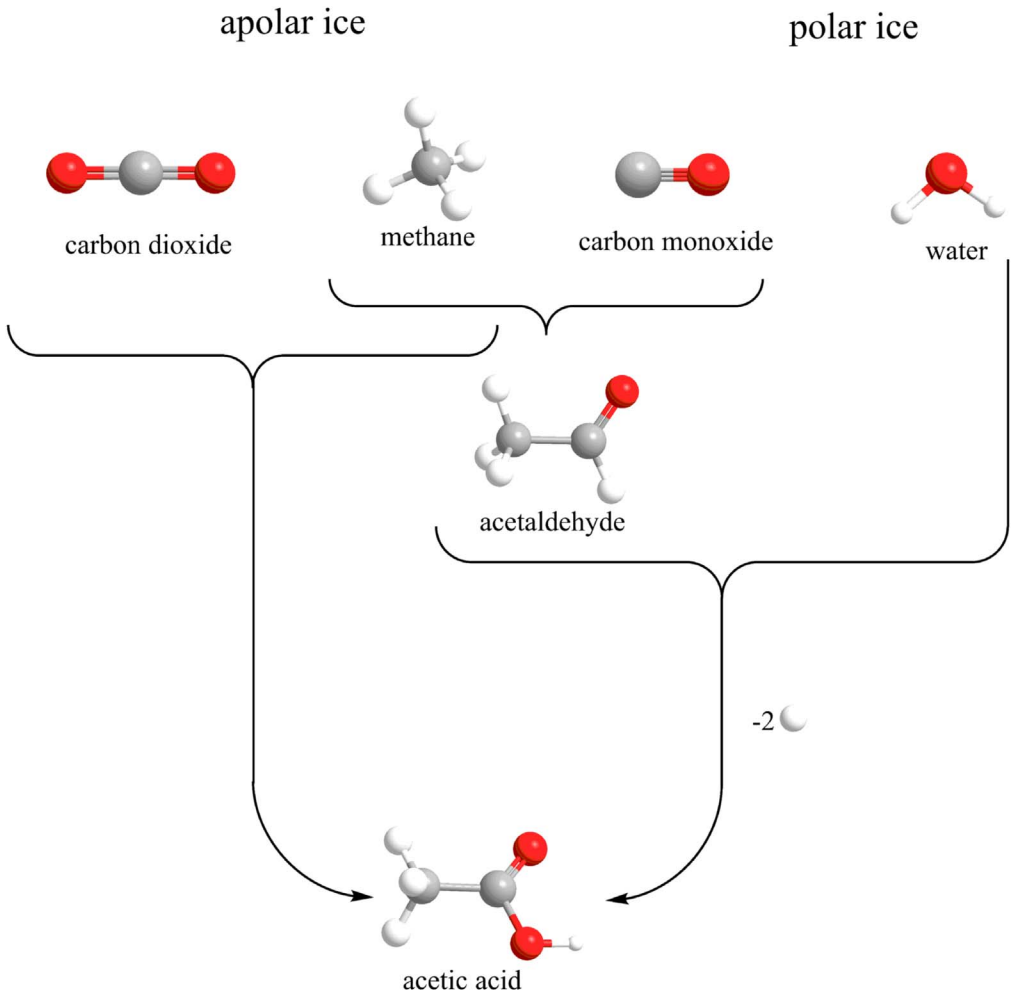

Figure 7. Reaction pathways leading to acetic acid in apolar and polar ices.

monoxide, which yielded glycolaldehyde and methyl formate after energetic processing (Bennett & Kaiser 2007b), the present system constitutes an *isomer-selective pathway* to the exclusive production of the acetic acid isomer (Figure 7). Through isotopic labeling we were also able to demonstrate that the formation pathway is the barrierless radical–radical reaction of acetyl and hydroxyl radicals, whereas insertion of excited singlet oxygen ($O(^1D)$) did not contribute to $C_2H_4O_2$ formation in detectable quantities. Most likely this is due to the fact that the $O(^1D)$ is easily quenched to the electronic ground ^3P state. This is indicated by the much shorter lifetime of the excited state in the solid state, which was determined to go down to less than a second in the solid state with a strong dependence on the ice composition (Mohammed 1990), whereas in the absence of collisions the excited state exhibits a lifetime of 135 s through radiative de-excitation (Baluja & Zeippen 1988). Therefore, unless the collision geometry is within the cone of acceptance for insertion reactions, the majority of $O(^1D)$ atoms will decay to their ground state. In contrast, the acetyl and hydroxyl radicals remain stable and isolated until their mobilities are high enough for them to assume favorable geometries and recombine with each other or other radicals, making this the dominant reaction pathway. This inefficient oxygen insertion is the reason for the isomer-selectivity of this reaction. It has been shown previously that acetaldehyde subjected to energetic electrons forms acetyl radicals but not vinoxy radicals (Kleimeier et al. 2020), which has been validated in the IR spectra in this study. Therefore, in the absence of oxygen insertion, the radical–radical recombination of acetyl and hydroxyl can only yield acetic acid as its product. The formation of its geminal diol, 1,1-ethenediol, is also not favored because the isomerization of acetaldehyde to form vinyl alcohol does not proceed in detectable amounts at the irradiation dose used in this experiment (Kleimeier et al. 2020). The overall reaction to form acetic acid and two hydrogen atoms from water and acetaldehyde is endoergic ($\Delta_r G = 415\,\mathrm{kJ\,mol^{-1}}$, reaction (12)); hence the overall formation of acetic acid must be a non-equilibrium reaction. The energy necessary for the reaction to proceed can be supplied by energy transfer processed from the secondary electrons in the track of GCRs as demonstrated in this study.

To conclude, these experiments demonstrate an isomer-selective pathway to acetic acid formation in polar ice mixtures composed of heavy water and acetaldehyde subjected to energetic electrons simulating secondary electrons in the track of GCRs. The acetic acid molecule and fragments of its dimer were positively identified by employing photoionization reflectron time-of-flight mass spectrometry in combination with temperature-programmed desorption. By tuning the photon energy of the ionization source, other isomers at the same mass-to-charge ratio could be ruled out as contributors to the signal. Once the acetaldehyde content of interstellar ices is quantified, this newly unraveled, isomer-selective reaction pathway can be included in interstellar chemical models

aiming to replicate relative abundances of the detected $C_2H_4O_2$ isomers in different interstellar environments. Furthermore, based on the ionization energy and isotopic composition of the ice, the formation of formaldehyde from the barrierless radical–radical recombination of formyl and hydroxyl radicals and the formation of methanol from methyl and hydroxyl radicals could be confirmed in this experiment. The overall production rate of acetic acid in the polar ice mixture of $(4.4 \pm 3.6) \times 10^{-4}$ molecules eV^{-1} is comparable to that in apolar ices of carbon dioxide and methane of $(4.2 \pm 1.3) \times 10^{-4}$ molecules eV^{-1} (Bennett & Kaiser 2007a). Therefore, given that water is at least one order of magnitude more dominant in interstellar ices than methane, the production rate of acetic acid from the reaction of water and acetaldehyde can be expected to exceed that from the carbon dioxide/methane reaction in realistic interstellar ices.

Financial support from the US National Science Foundation (AST-1800975) is greatly acknowledged (N.F.K., R.I.K.). The experimental setup was financed by the W. M. Keck Foundation. N.F.K. acknowledges funding from the Deutsche Forschungsgemeinschaft (DFG, German Research Foundation) for a postdoctoral fellowship (KL 3342/1-1). A.K.E. thanks the Alexander von Humboldt Foundation for a Feodor Lynen Research Fellowship.

ORCID iDs

N. Fabian Kleimeier https://orcid.org/0000-0003-1767-897X
André K. Eckhardt https://orcid.org/0000-0003-1029-9272
Ralf I. Kaiser https://orcid.org/0000-0002-7233-7206

References

Abplanalp, M. J., Gozem, S., Krylov, A. I., et al. 2016, PNAS, 113, 7727
Alizadeh, E., Orlando, T. M., & Sanche, L. 2015, ARPC, 66, 379
Altwegg, K., Balsiger, H., Berthelier, J. J., et al. 2017, MNRAS, 469, S130
Baluja, K. L., & Zeippen, C. J. 1988, JPhB, 21, 1455
Bartlett, R. J., Watts, J. D., Kucharski, S. A., & Noga, J. 1990, CPL, 165, 513
Becke, A. D. 1988, PhRvA, 38, 3098
Becke, A. D. 1993, JChPh, 98, 5648
Bennett, C. J., Hama, T., Kim, Y. S., Kawasaki, M., & Kaiser, R. I. 2011, ApJ, 727, 27
Bennett, C. J., Jamieson, C. S., Osamura, Y., & Kaiser, R. I. 2005a, ApJ, 624, 1097
Bennett, C. J., & Kaiser, R. I. 2007a, ApJ, 660, 1289
Bennett, C. J., & Kaiser, R. I. 2007b, ApJ, 661, 899
Bennett, C. J., Osamura, Y., Lebar, M. D., & Kaiser, R. I. 2005b, ApJ, 634, 698
Bergantini, A., Abplanalp, M. J., Pokhilko, P., et al. 2018a, ApJ, 860, 108
Bergantini, A., Maksyutenko, P., & Kaiser, R. I. 2017, ApJ, 841, 96
Bergantini, A., Zhu, C., & Kaiser, R. I. 2018b, ApJ, 862, 140
Burke, D. J., Puletti, F., Brown, W. A., et al. 2014, MNRAS, 447, 1444
Cizek, J. 1966, JChPh, 45, 4256
Crovisier, J., Bockelée-Morvan, D., Colom, P., et al. 2004, A&A, 418, 1141
Dohnálek, Z., Kimmel, G. A., Ayotte, P., Smith, R. S., & Kay, B. D. 2002, JChPh, 118, 364
Drouin, D., Couture, A. R., Joly, D., et al. 2007, Scanning, 29, 92
Dunning, T. H., Jr 1989, JChPh, 90, 1007
Eckhardt, A. K., Bergantini, A., Singh, S. K., Schreiner, P. R., & Kaiser, R. I. 2019, Angew Chem Int Ed, 58, 5663
Ehrenfreund, P., & Charnley, S. B. 2000, ARA&A, 38, 427
Fang, W. H., Liu, R. Z., Zheng, X., & Phillips, D. L. 2002, JOC, 67, 8407
Favre, C., Pagani, L., Goldsmith, P., et al. 2017, A&A, 604, L2
Fourikis, N., Sinclair, M. W., Robinson, B. J., Godfrey, P. D., & Brown, R. D. 1974, AuJPh, 27, 425
Frisch, M. J., Trucks, G. W., Schlegel, H. B., et al. 2016, Gaussian 16, Revision A.03 (Wallingford, CT: Gaussian Inc.)
Garrod, R. T., Weaver, S. L. W., & Herbst, E. 2008, ApJ, 682, 283
Gibb, E. L., Whittet, D. C. B., Boogert, A. C. A., & Tielens, A. G. G. M. 2004, ApJS, 151, 35
Guan, J., Hu, Y., Zou, H., et al. 2012, JChPh, 137, 124308
Hilbig, R., & Wallenstein, R. 1983, IJQE, 19, 194
Hudson, R. L., & Coleman, F. M. 2019, PCCP, 21, 11284
Jacox, M. E. 1982, CP, 69, 407
Jones, B. M., & Kaiser, R. I. 2013, JPCL, 4, 1965
Jørgensen, J. K., Van der Wiel, M. H. D., Coutens, A., et al. 2016, A&A, 595, A117
Jungclaus, G. A., Yuen, G. U., Moore, C. B., & Lawless, J. G. 1976, Metic, 11, 231
Kaiser, R. I., Eich, G., Gabrysch, A., & Roessler, K. 1997, ApJ, 484, 487
Kaiser, R. I., Maity, S., & Jones, B. M. 2014, PCCP, 16, 3399
Kaiser, R. I., & Roessler, K. 1997, ApJ, 475, 144
Kaiser, R. I., & Roessler, K. 1998, ApJ, 503, 959
Kaiser, R. I., Stockton, A. M., Kim, Y. S., Jensen, E. C., & Mathies, R. A. 2013, ApJ, 765, 111
Kim, Y. S., & Kaiser, R. I. 2010, ApJ, 725, 1002
Kleimeier, N. F., Turner, A. M., Fortenberry, R. C., & Kaiser, R. I. 2020, ChPhC, 21, 1531
Lee, C., Yang, W., & Parr, R. G. 1988, PhRvB, 37, 785
Lias, S. G. 2020, in NIST Chemistry WebBook, ed. P. J. Linstrom & W. G. Mallard (Gaithersburg, MD: National Institute of Standards and Technology)
Maity, S., Kaiser, R. I., & Jones, B. M. 2014, FaDi, 168, 485
Maity, S., Kaiser, R. I., & Jones, B. M. 2015, PCCP, 17, 3081
Mardyukov, A., Eckhardt, A. K., & Schreiner, P. R. 2020, Angew Chem Int Ed, 59, 5577
Matthews, H. E., Friberg, P., & Irvine, W. M. 1985, ApJ, 290, 609
Mehringer, D. M., Snyder, L. E., Miao, Y., & Lovas, F. J. 1997, ApJL, 480, L71
Mohammed, H. H. 1990, JChPh, 93, 412
Moore, M. H., & Hudson, R. L. 1998, Icar, 135, 518
Mottl, M. J., Glazer, B. T., Kaiser, R. I., & Meech, K. J. 2007, Geoch, 67, 253
Nummelin, A., Dickens, J. E., Bergman, P., et al. 1998, A&A, 337, 275
Öberg, K. I., Boogert, A. C. A., Pontoppidan, K. M., et al. 2011, ApJ, 740, 109
Öberg, K. I., Garrod, R. T., van Dishoeck, E. F., & Linnartz, H. 2009, A&A, 504, 891
Öberg, K. I., van Dishoeck, E. F., Linnartz, H., & Andersson, S. 2010, ApJ, 718, 832
Peterson, K. A., Woon, D. E., & Dunning, T. H. 1994, JChPh, 100, 7410
Porterfield, J. P., Baraban, J. H., Troy, T. P., et al. 2016, JPCA, 120, 2161
Puletti, F., Malloci, G., Mulas, G., & Cecchi-Pestellini, C. 2010, MNRAS, 402, 1667
Raghavachari, K. 1991, ARPC, 42, 615
Remijan, A., Snyder, L. E., Friedel, D. N., Liu, S.-Y., & Shah, R. Y. 2003, ApJ, 590, 314
Remijan, A., Snyder, L. E., Liu, S.-Y., Mehringer, D., & Kuan, Y.-J. 2002, ApJ, 576, 264
Roessler, K. 1992, NIMPB, 65, 55
Schuhmann, M., Altwegg, K., Balsiger, H., et al. 2019, ESC, 3, 1854
Schutte, W. A., Boogert, A. C. A., Tielens, A. G. G. M., et al. 1999, A&A, 343, 966
Schutte, W. A., Greenberg, J. M., van Dishoeck, E. F., et al. 1998, Ap&SS, 255, 61
Shiao, Y.-S. J., Looney, L. W., Remijan, A. J., Snyder, L. E., & Friedel, D. N. 2010, ApJ, 716, 286
Stanton, J. F. 1997, CPL, 281, 130
Tao, W., Klemm, R. B., Nesbitt, F. L., & Stief, L. J. 1992, JPhCh, 96, 104
Tureček, F., & Havlas, Z. 1986, J Chem Soc Perkin, 2, 1011
Turner, A. M., Abplanalp, M. J., Chen, S. Y., et al. 2015, PCCP, 17, 27281
Turner, B. E., Terzieva, R., & Herbst, E. 1999, ApJ, 518, 699
Wlodarczak, G., & Demaison, J. 1988, A&A, 192, 313
Xue, C., Remijan, A. J., Brogan, C. L., et al. 2019, ApJ, 882, 118
Yeghikyan, A. 2011, Ap, 54, 87
Zheng, W., Jewitt, D., & Kaiser, R. I. 2006a, ApJ, 639, 534
Zheng, W., Jewitt, D., & Kaiser, R. I. 2006b, ApJ, 648, 753
Zheng, W., Jewitt, D., & Kaiser, R. I. 2007, CPL, 435, 289
Zhu, C., Turner, A. M., Abplanalp, M. J., & Kaiser, R. I. 2018, ApJS, 234, 15
Zhu, R. S., Diau, E. G. W., Lin, M. C., & Mebel, A. M. 2001, JPCA, 105, 11249